

Pump Probe Spectroscopy of Polarons and Evidence for Thermalization

S.I. Mistakidis,¹ G.C. Katsimiga,¹ G.M. Koutentakis,^{1,2} Th. Busch,³ and P. Schmelcher^{1,4}

¹*Center for Optical Quantum Technologies, Department of Physics,
University of Hamburg, Luruper Chaussee 149, 22761 Hamburg Germany*

²*The Hamburg Centre for Ultrafast Imaging, University of Hamburg,
Luruper Chaussee 149, 22761 Hamburg, Germany*

³*OIST Graduate University, Onna, Okinawa 904-0495, Japan*

⁴*The Hamburg Centre for Ultrafast Imaging, Universität Hamburg,
Luruper Chaussee 149, 22761 Hamburg, Germany*

(Dated: January 3, 2020)

A pump-probe spectroscopy scheme is proposed in order to unveil the time-resolved dynamics of either fermionic or bosonic impurities immersed in a harmonically trapped Bose-Einstein condensate. Pump and probe pulses are utilized with the former transferring the impurities from a noninteracting to the polaronic state. The latter, being applied after variable dark times, allows to directly monitor the nonequilibrium dynamics of the impurities. Coherent attractive or repulsive Fermi and Bose polarons and their induced-interactions are evidenced in the probe spectra for moderate attractive and repulsive interspecies interactions. For strong repulsions an orthogonality catastrophe occurs independently of the impurity's flavour and it is found to be rather rapid for two impurities. In this case and for longer time scales a steady state is reached characterized by substantial coherence losses of the impurities which acquire an effectively large temperature. This steady state is related to an eigenstate thermalization which is shown to be independent of the system's characteristics.

Introduction.— The dynamical response of an atomic vapor upon its exposure to both a pump and a probe field, lies at the heart of nonlinear spectroscopy. Two-level and Λ -shaped three-level atomic systems have been studied via pump-probe spectroscopy (PPS) both theoretically [1–3] and experimentally [4, 5]. This allowed for the occurrence of stimulated emission instead of absorption upon strong pumping in nearly resonant driven systems [1], and the determination of the Bloch-Siegert shift [2]. Additionally via coherent population trapping, subwavelength localization of excited atomic states has been demonstrated [6, 7]. Moreover, utilizing PPS in a system of ultracold ⁸⁵Rb atoms gives rise to new features that are absent in two-level systems [5] such as the observation of selectively coherence-induced gain at the probe field frequency. Remarkably, and also very recently a PPS experiment [6] revealed that short-range anticorrelations between repulsively interacting fermions prevail against pairing processes whilst at long times a short-range correlated state has been identified. In this experiment, the strong pumping used gave access to the location of the atomic peak resonance. The latter entails important information of the relevant quasiparticle formation which thus far has not been explored utilizing PPS.

Accordingly, the understanding of the underlying correlated dynamics and interactions of attractive and repulsive Fermi [1, 2, 9–16, 18–24, 26–28] or Bose polarons [29–49] is of mandatory importance. This is corroborated by the importance of quasiparticle formation and dynamics in semiconducting [50] and superconducting devices [51] while interactions among quasiparticles in liquid Helium

mixtures [52, 53] and cuprates [54] are hold responsible for superconductivity. Deepening our current understanding of correlated interacting many-body (MB) systems by studying simpler models all the way from weak to strong interactions is an intriguing prospect. It is an open question if the time-resolved dynamics of bosonic and fermionic impurities can, at short time scales, provide direct access to their decoherence properties and whether at longer times a unified behavior, i.e independent of the statistics, towards an anticipated thermalized state exists [55, 56]. These results pave the way for probing and controlling the correlation properties of quasiparticles as it has been demonstrated recently in the context of polaritons [57, 58].

In this Letter we address the above questions by utilizing a PPS radiofrequency scheme analogous to the experiment of Ref. [6] mimicking ultrafast spectroscopic techniques applied in solid state [59, 60]. Initially, an intense pump pulse transfers the bosonic or fermionic impurities from the noninteracting ground state to either the attractive or the repulsively interacting state. Then, a weaker intensity probe pulse applied after a variable dark time captures the time evolution as the impurities are selectively deexcited. Well-defined attractive and repulsive Fermi and Bose polarons are monitored in the probe spectra that are long lived up to moderate interspecies repulsions. For stronger repulsions substantial losses of coherence occur and the orthogonality catastrophe of the polarons is imprinted in the spectrum. This process appears from the initial stages of the nonequilibrium dynamics independently of one or two impurities and their flavour. Remarkably, at longer evolution times the probe

spectrum unveils evidences towards the eigenstate thermalization of the impurities [10, 11], which reside in an incoherent state characterized by a large effective temperature. This relaxation tendency is found to be independent of the sizes of the bath, number and flavour of the impurities, their interactions and mass.

Model.— Our model is a highly particle imbalanced mixture. It consists of $N_I = 1, 2$ bosonic or fermionic impurities (I) having a spin-1/2 degree of freedom [28] being immersed in a bosonic bath of $N_B = 100$ structureless bosons (B). The mixture is assumed to be mass balanced, $m_B = m_I$ (unless stated otherwise), while both species are harmonically confined in the same one-dimensional external potential of frequency $\omega = 1$. The MB Hamiltonian reads

$$\hat{H} = \hat{H}_B^0 + \hat{H}_{BB} + \sum_{a=\uparrow, \downarrow} (\hat{H}_a^0 + \hat{H}_{aa}) + \hat{H}_{\uparrow\downarrow} + \hat{H}_{BI} + \hat{H}_S^\beta. \quad (1)$$

Here, $\hat{H}_B^0 = \int dx \hat{\Psi}_B^\dagger(x) \left(-\frac{\hbar^2}{2m_B} \frac{d^2}{dx^2} + \frac{1}{2} m_B \omega^2 x^2 \right) \hat{\Psi}_B(x)$, and $\hat{H}_a^0 = \int dx \hat{\Psi}_a^\dagger(x) \left(-\frac{\hbar^2}{2m_I} \frac{d^2}{dx^2} + \frac{1}{2} m_I \omega^2 x^2 \right) \hat{\Psi}_a(x)$ denote the noninteracting Hamiltonian of the BEC and the impurities respectively while $a \in \{\uparrow, \downarrow\}$. Additionally, $\hat{\Psi}_B(x)$ [$\hat{\Psi}_a(x)$] is the field-operator of the BEC [spin- a impurities]. We further consider that the dominant interaction is an s -wave one since we operate in the ultracold regime. As such both intra- (g_{BB} , g_{II}) and inter-species (g_{BI}) interactions are adequately described by a contact potential. Furthermore, $\hat{H}_{BB} = g_{BB} \int dx \hat{\Psi}_B^\dagger(x) \hat{\Psi}_B^\dagger(x) \hat{\Psi}_B(x) \hat{\Psi}_B(x)$ and $\hat{H}_{aa'} = g_{II} \int dx \hat{\Psi}_a^\dagger(x) \hat{\Psi}_{a'}^\dagger(x) \hat{\Psi}_{a'}(x) \hat{\Psi}_a(x)$, with $a, a' \in \{\uparrow, \downarrow\}$, corresponding to the contact intraspecies interaction terms of the bosonic bath and the impurities respectively. Note that only the spin- \uparrow component of the impurities interacts with the BEC while the spin- \downarrow one is noninteracting. The relevant interspecies interaction term reads $\hat{H}_{BI} = g_{BI} \int dx \hat{\Psi}_B^\dagger(x) \hat{\Psi}_\uparrow^\dagger(x) \hat{\Psi}_\uparrow(x) \hat{\Psi}_B(x)$. Finally, $\hat{H}_S^\beta = \frac{\hbar \Omega_{R0}^\beta}{2} \hat{S}_x - \frac{\hbar \Delta^\beta}{2} \hat{S}_z$, with Ω_{R0}^β and $\Delta^\beta = \nu^\beta - \nu_0$ referring to the bare Rabi frequency and the detuning of the radiofrequency pulse with $\beta \in \{\text{pump}, \text{probe}, \text{dark}\}$ when the bosonic bath is absent [67]. Moreover, the total spin operator is given by $\hat{S} = \int dx \sum_{ab} \hat{\Psi}_a(x) \boldsymbol{\sigma}_{ab} \hat{\Psi}_b(x)$, with $\boldsymbol{\sigma}$ denoting the Pauli vector.

To access the time-resolved spectral response of bosonic and fermionic impurities immersed in the BEC bath the Multilayer Multi-Configuration Time-Dependent Hartree method for atomic mixtures is utilized [21, 65, 66]. The latter is a nonperturbative approach that uses a variationally optimized time-dependent basis which spans the optimal subspace of the Hilbert space at each time instant and allows for tackling all interatomic correlations [67]. To trigger the nonequilibrium dynamics, we prepare the multicomponent system in its ground state with $g_{II} = 0$ and the spin degrees

of freedom fixed to their spin- \downarrow state, corresponding to a fixed g_{BB} and $\langle \hat{H}_{BI} \rangle = 0$. For $-t_e < t < 0$ (where t_e denotes the exposure time), an intense, $\Omega_{R0}^{\text{pump}} = 10$, rectangular pump pulse resonantly populates the polaronic states by driving the $|\downarrow\rangle$ noninteracting impurities to their interacting $|\uparrow\rangle$ state [Fig. 1(a)]. To ensure the resonance condition of the pump pulse, namely $\Delta^{\text{pump}} = \Delta_+$, and to optimize $t_e = \pi/\Omega_R^{\text{pump}}$ the fraction of impurity atoms that have been successfully transferred to the polaronic $|\uparrow\rangle$ -state, $\langle N_\uparrow(t=0) \rangle / N_I$, is monitored for variable Δ^{pump} [Fig. 1(b)]. A coherent atomic resonance at $\Delta^{\text{pump}} = \Delta_+$ entailing the relevant information of the energy and effective mass of the well-defined attractive and repulsive polaronic states [2, 6, 22, 28, 46] is identified for $g_{BI} = -0.5, 0.5$ and 1.5 when $N_I = 1$ [Fig. 1(b)]. Note that secondary peaks possessing an intensity of the order of 12% of the polaronic ones also emerge [Fig. 1(b)] due to the rectangular shape of the pump pulse [67]. After the initial pump sequence the resulting population of the spin- \downarrow state is annihilated by employing an optical blast that projects the impurities to the $|\uparrow\rangle$ state [67] and subsequently the spin- \uparrow atoms are left to evolve for fixed g_{BI} and $\Omega_{R0}^{\text{dark}} = 0$ but variable dark time t_d . At the end of this dark time the nonequilibrium dynamics of the impurities is directly followed by applying a probe pulse [Fig. 1(a)]. This pulse is characterized by $\Omega_{R0}^{\text{probe}} = 1 \ll \Omega_{R0}^{\text{pump}}$ so as to enhance the spectral resolution of the signal obtained by the fraction of impurity atoms transferred to the spin- \downarrow state, $\langle N_\downarrow(t_d) \rangle / N_I$ for variable Δ^{probe} . For the same reason the duration of the probe pulse is fixed to $t'_e = \pi/\Omega_R^{\text{probe}}$ where Ω_R^{probe} is the resonant Rabi frequency of the probe pulse at $\Delta^{\text{probe}} = \Delta_+$, $t_d = 0$ and $N_I = 1$.

Results and Discussion.— The short-time dynamics of few, $N_I = 1, 2$, fermionic or bosonic impurities with $g_{II} = 0$ immersed in a BEC bath of $N_B = 100$ atoms, is captured by the probe spectra for distinct attractive [Figs. 1(c)-(e)] and repulsive [Figs. 1(f)-(k)] interspecies interactions g_{BI} . Focusing on the attractive side, a well-defined polaron at $t_d = 0$ with central peak location at $\Delta_+ = -8.7$ [Fig. 1(c)], $\Delta_{+,B} = -8.9$ [Fig. 1(d)], and $\Delta_{+,F} = -8.6$ [Fig. 1(e)] is identified in the cases of $N_I = 1$, and $N_I = 2$ bosonic and fermionic impurities respectively. These polarons show a nonsizable shift for all the different evolution times t_d as long as $N_I = 1$. However, a clear shift can be inferred for $N_I = 2$ [Fig. 1(d)]. This shift, being of about 10%, is a consequence of the energy redistribution between the bosonic impurities and the BEC as demonstrated in [46] and it is further related to the fact that for $g_{BI} < 0$ attractive induced-interactions are significantly enhanced [46]. Additionally, due to the pronounced induced-interactions a collisional broadening [68] of the spectral line is clearly observed for $t_d = 1, 11$. Indeed, since the two-body state of the impurities evolves rapidly during the probe sequence

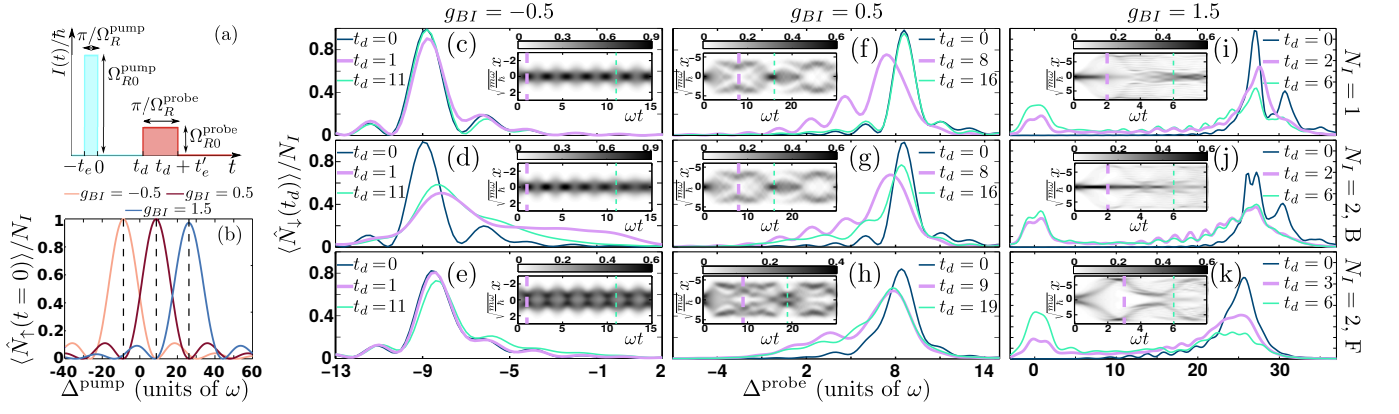


FIG. 1. (a) Schematic illustration of the PPS pulse sequences used. (b) Spectral response of the pump pulse $\langle \hat{N}_\uparrow(t=0) \rangle / N_I$ versus its detuning Δ_{pump} for $g_{BB} = 0.5$, $N_B = 100$, $N_I = 1$, $\omega = 1$ and varying g_{BI} . Vertical dashed lines indicate the resonant detunings Δ_+ . (c)-(k) Time-resolved probe spectra at different g_{BI} , bosonic (B) or fermionic (F) impurity numbers $N_I = 1, 2$ with $g_{II} = 0$, and for various short dark times, t_d (see legend). In all cases insets illustrate the spatiotemporal evolution of the impurity's one-body density and dashed lines mark the instants for which the probe spectrum is provided.

the spectral resolution of the measurement decreases giving rise to a wide background in the PPS spectrum for $-10 < \Delta_{\text{probe}} < 2$. The imprint of induced-interactions in the spatiotemporal evolution of the one-body density is the dephasing of the breathing oscillations [hardly visible in the inset of Fig. 1(d)] within the time interval $10 < t_d < 15$, which is absent for the single impurity [see the inset in Fig. 1(c)]. In contrast to the above dynamics, the time-resolved evolution of Fermi polarons closely resembles the single impurity one with the two fermions undergoing at short times a coherent breathing motion, see the inset in Fig. 1(e). This latter result can be easily understood by the fact that attractive induced-interactions between fermionic impurities are known to be suppressed providing in turn a nonsizeable shift of the respective atomic peak resonance captured by the probe spectra [2, 28].

Switching to repulsive interactions, the dynamical evolution of the system changes dramatically. Independently of flavour and concentration the motion of the impurities, as detected by the one-body density evolution for $g_{BI} = 0.5$, is apparently qualitatively similar [insets in Figs. 1(f)-1(h)]. From the very early stages of the nonequilibrium dynamics the density filamentizes with recurrences of an almost central density peak occurring at the collision points, i.e. around $t_d \approx 16$ and $t_d \approx 18$ for the bosonic and fermionic impurities respectively [Fig. 1(g) and Fig. 1(h)]. However in all three cases a clean quasiparticle peak is monitored in the respective probe spectra indicating the existence of well-defined polarons for these short times. The dominant peak location appears to be shifted for $t_d \neq 0$ when compared to Δ_+ , while an overall broadening of the pulse is also inferred. The observed shift is independent of the number of impurities [compare Figs. 1(f) and 1(g)] but depends strongly on the impurity's nature with the shift mea-

sured to be of about 10% for Bose but dropping down to almost 5% for Fermi polarons [Figs. 1(g), 1(h)]. These findings suggest that attractive induced-interactions cannot be directly unveiled by the observed shift. A result that complements earlier predictions indicating that attractive induced-interactions are suppressed in the repulsive regime [15, 70]. In turn by inspecting the oscillatory tail of the probe spectra for $g_{BI} > 0$ interference phenomena associated with the filamentation process can be identified. Indeed, already from the single impurity [Fig. 1(f)] the amplitude, $A(\Delta^{\text{probe}})$, of the secondary peak appearing in the spectra e.g. at $t_d = 8$, $A(\Delta^{\text{probe}} \approx 4.6) = 0.3518$ is comparable with the dominant one $A(\Delta^{\text{probe}} \approx 7.5) = 0.755$. Notice that the intensity ratio of the secondary to the dominant peak is $> 12\%$ and thus cannot be attributed to the rectangular shape of the probe pulse. The latter, directly reflects the coherence between the filaments formed in the one-body density (see discussion below). However, as the number of impurities increases significant losses of coherence take place. Indeed, the secondary peak at $t_d = 8$ [$t_d = 9$] has $A(\Delta^{\text{probe}} \approx 4.6) = 0.266$ [$A(\Delta^{\text{probe}} \approx 3.6) = 0.245$] for $N_I = 2$ bosonic [fermionic] impurities while is drastically reduced at later t_d [Figs. 1(g), 1(h)]. From the above discussion, it becomes apparent that two competing mechanisms are into play. Attractive-induced interactions and loss of coherence render the dynamics far more complicated in the repulsive regime. Moreover among these mechanisms it seems that loss of coherence dominates, hindering this way the presence of induced-interactions.

Our PPS data demonstrate that well-defined quasiparticles cease to exist for $g_{BI} \gtrsim 1.5$ signaling their orthogonality catastrophe [Figs. 1(i)-(k)] [46]. Evidently, at $t_d = 0$ a predominant peak centered at $\Delta_+ = 26.7$ can be discerned in the single impurity probe spectrum [Fig. 1(i)], giving its place to a double humped struc-

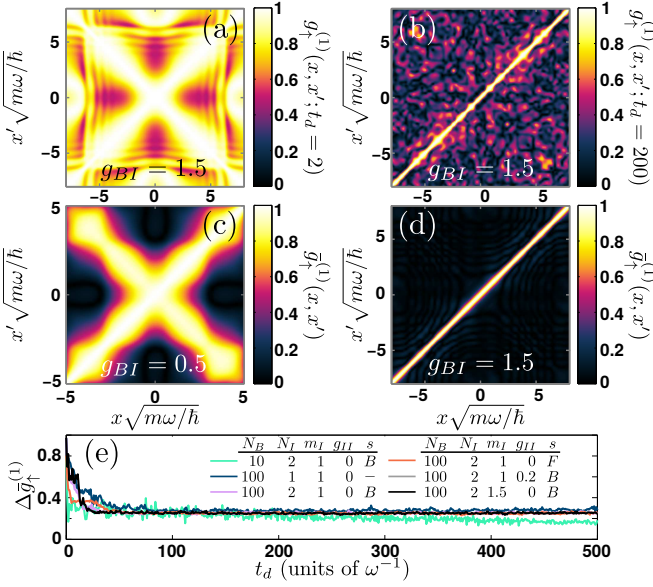


FIG. 2. (a), (b) One-body coherence $g_+^{(1)}(x, x'; t_d)$ at different times t_d (see legend). (c), (d) Time-averaged one-body coherence $\bar{g}_+^{(1)}(x, x')$ at distinct g_{BI} . (e) Temporal evolution of the variance $\Delta \bar{g}_+^{(1)}$ for different settings (see legend).

ture with averaged location at $\Delta_{+,B} = 26.75$ for the two bosonic impurities [Fig. 1(j)], and to a slightly shifted but significantly broadened peak at $\Delta_{+,F} = 25.6$ for the fermionic ones [Fig. 1(k)]. The latter broadening is attributed to the fermion statistics. Indeed fermionic impurities occupy higher momenta and as such interact more weakly with the BEC bath [67]. However, at $t_d = 2$ deformation of the central peak is present and a highly oscillatory tail is seen in all cases. To appreciate the aforementioned degree of coherence already indicated by the probe spectra we next invoke the spatial first order coherence function $g_\sigma^{(1)}(x, x'; t) = \rho_\sigma^{(1)}(x, x'; t) / \sqrt{\rho_\sigma^{(1)}(x; t) \rho_\sigma^{(1)}(x'; t)}$. Here, $\rho_\sigma^{(1)}(x, x'; t)$ is the σ -species ($\sigma = B, I$) one-body reduced density matrix and $\rho_\sigma^{(1)}(x; t)$ is the one-body density [67]. Importantly, $|g_\sigma^{(1)}(x, x'; t)| \in [0, 1]$ indicates the spatially resolved deviation of a MB wavefunction from a corresponding product state. Specifically, if $|g_\sigma^{(1)}(x, x'; t)| = 1$ the system is termed fully coherent otherwise coherence losses occur signifying the build-up of correlations [15, 71]. Indeed, the instantaneous $|g_+^{(1)}(x, x'; t_d = 2)|$ for $g_{BI} = 1.5$ clearly dictates that the quasiparticle remains adequately coherent since e.g. $|g_+^{(1)}(x = -5, x' = 5; t_d = 2)| \approx 0.96$ [Fig. 2(a)]. Finally, notice that for $t_d > 6$ any quasiparticle notion is lost as detected by the probe spectra. This outcome, being consistent with recent works [28, 46], is also supported by the diffusive behaviour of the corresponding one-body density evolution [insets in Figs. 1(i)-1(k)]. In contrast, a peak corresponding to free particles

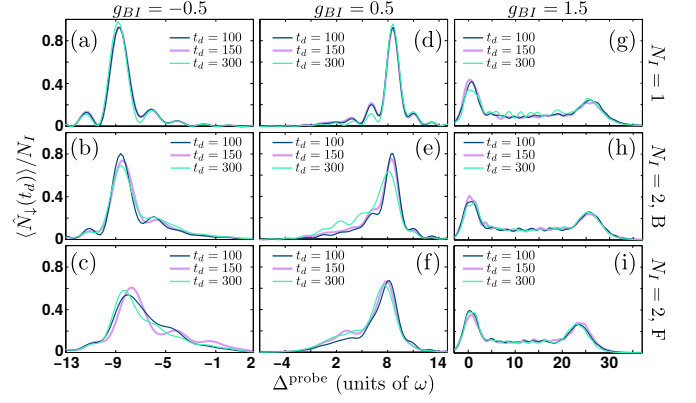


FIG. 3. (a)-(i) Probe spectra for different g_{BI} , N_I , and impurity flavours at various dark times t_d deep in the evolution (see legend).

$\Delta^{\text{probe}} = 0$ emanates in the PPS spectrum, referring to the accumulation of impurity density outside the BEC with Thomas-Fermi radius $R_{TF} \approx 4.2$.

Next let us study the evolution of the system at longer times $100 < t_d < 300$ [72]. As time evolves one expects that significant losses of coherence signaling the build-up of correlations will take place in the MB evolution of the system [Fig. 2(b)]. A powerful asset of exposing the latter is the temporal average $\bar{g}_+^{(1)}(x, x') = \lim_{T \rightarrow \infty} \frac{1}{T} \int_0^T dt g_+^{(1)}(x, x'; t)$ which is only dependent on the eigenstate properties of the interacting system [73]. This allows us to infer the relaxation tendency of the impurities within the framework of eigenstate thermalization hypothesis [10, 11, 67]. Evidently, $\bar{g}_+^{(1)}(x, x')$ reveals that for $g_{BI} = 0.5$ the impurity is largely coherent [Fig. 2(c)] whilst at $g_{BI} = 1.5$ any coherence property is lost [Fig. 2(d)]. This outcome is further supported by the time-resolved probe spectra illustrated for longer times in Figs. 3(a)-3(i). A strong suppression of the interaction shift with respect to Δ_+ is found to persist at long times which together with the weakly fluctuating amplitude $A(\Delta^{\text{probe}} \approx \Delta_+)$ observed in the course of time verifies the longevity of coherent single and two polarons irrespectively of their flavour and for both attractive and moderate repulsive g_{BI} [Figs. 3(a)-3(f)]. Alterations come into play for stronger repulsions where as per our discussion above losses of coherence, as captured by $g_+^{(1)}(x, x'; t_d)$, become significant and the polaron picture breaks down. Here, a two-humped distribution that appears to be independent of the number of the impurities and their nature is monitored in our probe spectra, with the most pronounced feature being the peak located at $\Delta^{\text{probe}} = 0$ [Figs. 3(g)-3(i)]. The latter findings suggest that a relaxed state is reached characterized by incoherent impurities being unpredicted so far. Indeed, by fitting $\bar{g}_+^{(1)}(x, x')$ to the corresponding prediction of

the N_I -particle Gibbs ensemble we obtain large effective temperatures. These refer to $k_B T_{\text{eff}} = 8.45\hbar\omega$ for $N_I = 1$ and $k_B T_{\text{eff}} = 8.58\hbar\omega$ ($k_B T_{\text{eff}} = 5.89\hbar\omega$) in the case of two bosons (fermions) showcasing their tendency to approach an incoherent thermalized state [67]. Notice that the initial state of fermions involves higher momenta than bosons, while the critical velocity of the BEC is the same [74–76]. Therefore, fermions couple stronger to the BEC excitations losing a larger portion of their energy implying a smaller T_{eff} . Further evidences supporting the observed thermalization [55, 56] are provided by the temporal evolution of the variance $\Delta\bar{g}_{\uparrow}^{(1)} = (TS)^{-1} \int_S dx dx' \int dt \left[g_I^{(1)}(x, x'; t) - \bar{g}_I^{(1)}(x, x') \right]^2 \in (0, 1)$, with S denoting the relevant spatial region in which the impurities reside. Remarkably a tendency towards thermalization is seen [Fig. 2(e)], irrespectively of the size of the BEC medium interacting or noninteracting impurities, and also independently of one or two impurities and their nature, with $\Delta\bar{g}_{\uparrow}^{(1)}$ saturating at long times for all the distinct setups [67].

Conclusions.— A PPS scheme is utilized to study the correlated time-resolved dynamics of fermionic and bosonic impurities immersed in a harmonically confined BEC. Coherence properties and induced-interactions are encoded in the probe spectra revealing that the latter dominate the former and vice versa when crossing from the attractive to the repulsive regime of interactions. Nevertheless, coherent attractive and repulsive polarons of different flavour exist up to moderate interspecies repulsions. For strong repulsions, where any coherence information is lost, a rather rapid orthogonality catastrophe occurs. Astonishingly, at longer times a thermalized state is reached. This thermalization is independent of the size of the bath and the impurity's concentration, the interacting nature of the impurities as well as their flavour and mass. It would be intriguing to utilize PPS in the presence of temperature [77, 78] and also in higher dimensions [79] to explore whether or not thermalization can be inferred.

P.S. and G.M.K gratefully acknowledge funding by the Cluster of Excellence 'CUI: Advanced Imaging of Matter' of the Deutsche Forschungsgemeinschaft (DFG) - EXC 2056 - project ID 390715994. S.I.M. gratefully acknowledges financial support in the framework of the Lenz-Ising Award of the University of Hamburg. T.B. has been supported by the Okinawa Institute of Science and Technology Graduate University.

G.C.K, S.I.M. and G.M.K. contributed equally to this work.

[1] B. R. Mollow, Phys. Rev. A **5**, 2217 (1972).

[2] C. Wei, A. S. Windsor, and N. B. Manson, J. Phys. B: Atom. Mol. Opt. Phys. **30**, 4877 (1997).
[3] P. R. Berman, and B. Dubetsky, Phys. Rev. A **62**, 053412 (2000).
[4] F. Y. Wu, S. Ezekiel, M. Ducloy, and B. R. Mollow, Phys. Rev. Lett. **38**, 1077 (1977).
[5] A. K. Mills, and D. S. Elliott, Phys. Rev. A **86**, 063819 (2012).
[6] A. V. Gorshkov, L. Jiang, M. Greiner, P. Zoller, and M. D. Lukin, Phys. Rev. Lett. **100**, 093005 (2008).
[7] H. Li, V. A. Sautenkov, M. M. Kash, A. V. Sokolov, G. R. Welch, Y. V. Rostovtsev, M. S. Zubairy, and M. O. Scully, Phys. Rev. A **78**, 013803 (2008).
[8] A. Amico, F. Scazza, G. Valtolina, P. E. S. Tavares, W. Ketterle, M. Inguscio, G. Roati, and M. Zaccanti, Phys. Rev. Lett. **121**, 253602 (2018).
[9] A. Schirotzek, C.-H. Wu, A. Sommer, and M. W. Zwierlein, Phys. Rev. Lett. **102**, 230402 (2009).
[10] S. Nascimbène, N. Navon, K. J. Jiang, L. Tarruell, M. Teichmann, J. McKeever, F. Chevy, and C. Salomon, Phys. Rev. Lett. **103**, 170402 (2009).
[11] M. Punk, P. T. Dumitrescu, and W. Zwerger, Phys. Rev. A **80**, 053605 (2009).
[12] F. Chevy, and C. Mora, Rep. Prog. Phys. **73**, 112401 (2010).
[13] X. Cui, and H. Zhai, Phys. Rev. A **81**, 041602(R) (2010).
[14] S. Pilati, G. Bertaina, S. Giorgini, and M. Troyer, Phys. Rev. Lett. **105**, 030405 (2010).
[15] P. Massignan, and G. Bruun, Eur. Phys. J. D **65**, 83 (2011).
[16] R. Schmidt, and T. Enss, Phys. Rev. A **83**, 063620 (2011).
[17] C. Kohstall, M. Zaccanti, M. Jag, A. Trenkwalder, P. Massignan, G. M. Bruun, F. Schreck, and R. Grimm, Nature **485**, 615 (2012).
[18] M. Koschorreck, D. Pertot, E. Vogt, B. Fröhlich, M. Feld, and M. Köhl, Nature **485**, 619 (2012).
[19] R. Schmidt, T. Enss, V. Pietilä, and E. Demler, Phys. Rev. A **85**, 021602 (2012).
[20] V. Ngampruetikorn, J. Levinsen, and M. M. Parish, Europhys. Lett. **98**, 30005 (2012).
[21] P. Massignan, Z. Yu, and G. M. Bruun, Phys. Rev. Lett. **110**, 230401 (2013).
[22] P. Massignan, M. Zaccanti, and G. M. Bruun, Rep. Prog. Phys. **77**, 034401 (2014).
[23] E. Burovski, V. Cheianov, O. Gamayun, and O. Lychkovskiy, Phys. Rev. A **89**, 041601 (2014).
[24] M. Cetina, M. Jag, R. S. Lous, I. Fritsche, J. T. M. Walraven, R. Grimm, J. Levinsen, M. M. Parish, R. Schmidt, M. Knap, and E. Demler, Science **354**, 96 (2016).
[25] F. Scazza, G. Valtolina, P. Massignan, A. Recati, A. Amico, A. Burchianti, C. Fort, M. Inguscio, M. Zaccanti, and G. Roati, Phys. Rev. Lett. **118**, 083602 (2017).
[26] R. Schmidt, M. Knap, D. A. Ivanov, J. -S. You, M. Cetina, and E. Demler, Rep. Prog. Phys. **81**, 024401 (2018).
[27] O. Gamayun, O. Lychkovskiy, E. Burovski, M. Malcomson, V. V. Cheianov, and M. B. Zvonarev, Phys. Rev. Lett. **120**, 220605 (2018).
[28] S. I. Mistakidis, G. C. Katsimiga, G. M. Koutentakis, and P. Schmelcher, New J. Phys. **21**, 043032 (2019).
[29] S. Palzer, C. Zipkes, C. Sias, and M. Köhl, Phys. Rev. Lett. **103**, 150601 (2009).
[30] J. Tempere, W. Casteels, M. K. Oberthaler, S. Knoop,

- E. Timmermans, and J. T. Devreese, Phys. Rev. B **80**, 184504 (2009).
- [31] J. Catani, G. Lamporesi, D. Naik, M. Gring, M. Inguscio, F. Minardi, A. Kantian, and T. Giamarchi, Phys. Rev. A **85**, 023623 (2012).
- [32] T. Fukuhara, A. Kantian, M. Endres, M. Cheneau, P. Schauss, S. Hild, D. Bellem, U. Schollwöck, T. Giamarchi, C. Gross, I. Bloch, and S. Kuhr, Nat. Phys. **9**, 235 (2013).
- [33] R. Scelle, T. Rentrop, A. Trautmann, T. Schuster, and M. K. Oberthaler, Phys. Rev. Lett. **111**, 070401 (2013).
- [34] R. Schmidt, H. R. Sadeghpour, and E. Demler, Phys. Rev. Lett. **116**, 105302 (2016).
- [35] L. A. Peña Ardila, and S. Giorgini, Phys. Rev. A **94**, 063640 (2016).
- [36] F. Grusdt, R. Schmidt, Y. E. Shchadilova, and E. Demler, Phys. Rev. A **96**, 013607 (2017).
- [37] A. G. Volosniev, and H.-W. Hammer, Phys. Rev. A **96**, 031601 (2017).
- [38] N. E. Guenther, P. Massignan, M. Lewenstein, and G. M. Bruun, Phys. Rev. Lett. **120**, 050405 (2018).
- [39] D. Mayer, F. Schmidt, D. Adam, S. Haupt, J. Koch, T. Lausch, J. Nettersheim, Q. Bouton, and A. Widera, arXiv:**1805.01313** (2018).
- [40] N. B. Jørgensen, L. Wacker, K. T. Skalmstang, M. M. Parish, J. Levinsen, R. S. Christensen, G. M. Bruun, and J. J. Arlt, Phys. Rev. Lett. **117**, 055302 (2016).
- [41] M.-G. Hu, M. J. Van de Graaff, D. Kedar, J. P. Corson, E. A. Cornell, and D. S. Jin, Phys. Rev. Lett. **117**, 055301 (2016).
- [42] Y. E. Shchadilova, R. Schmidt, F. Grusdt, and E. Demler, Phys. Rev. Lett. **117**, 113002 (2016).
- [43] J. Levinsen, M. M. Parish, and G. M. Bruun, Phys. Rev. Lett. **115**, 125302 (2015).
- [44] R. S. Christensen, J. Levinsen, and G. M. Bruun, Phys. Rev. Lett. **115**, 160401 (2015).
- [45] F. Grusdt, K. Seetharam, Y. Shchadilova, and E. Demler, Phys. Rev. A **97**, 033612 (2018).
- [46] S. I. Mistakidis, A. G. Volosniev, N. T. Zinner, and P. Schmelcher, Phys. Rev. A **100**, 013619 (2019).
- [47] M. Drescher, M. Salmhofer, and T. Enss, Phys. Rev. A **99**, 023601 (2019).
- [48] S.I. Mistakidis, G.C. Katsimiga, G.M. Koutentakis, Th. Busch, and P. Schmelcher Phys. Rev. Lett. **122**, 183001 (2019).
- [49] S. I. Mistakidis, F. Grusdt, G. M. Koutentakis, and P. Schmelcher New J. Phys. **21**, 103026 (2019).
- [50] M. E. Gershenson, V. Podzorov, and A. F. Morpurgo, Rev. Mod. Phys. **78**, 973 (2006).
- [51] S. T. Ruggiero, and D. A. Rudman, eds., *Superconducting Devices* (Academic, Boston, 1990).
- [52] J. Bardeen, G. Baym, and D. Pines, Phys. Rev. **156**, 207 (1967).
- [53] G. Baym, and C. Pethick, *Landau Fermi-Liquid Theory: Concepts and Applications* (Wiley-VCH, 1991).
- [54] D. J. Scalapino, Phys. Rep. **250**, 329 (1995).
- [55] T. Lausch, A. Widera, and M. Fleischhauer, Phys. Rev. A **97**, 033620 (2018).
- [56] T. Lausch, A. Widera, and M. Fleischhauer, Phys. Rev. A **97**, 023621 (2018).
- [57] N. Takemura, S. Trebaol, M. Wouters, M. T. Portella-Oberli, and B. Deveaud, Nat. Phys. **10**, 500 (2014).
- [58] M. Navadeh-Toupchi, N. Takemura, M.D. Anderson, D.Y. Oberli, and M.T. Portella-Oberli, Phys. Rev. Lett. **122**, 047402 (2019).
- [59] J. Orenstein, Phys. Today **65**, No. 9, 44 (2012).
- [60] C. Giannetti, M. Capone, D. Fausti, M. Fabrizio, F. Parmigiani, and D. Mihailovic, Adv. Phys. **65**, 58 (2016).
- [61] M. Rigol, V. Dunjko, and M. Olshanii, Nat. **452**, 854 (2008).
- [62] M. Rigol, and M. Srednicki, Phys. Rev. Lett. **108**, 110601 (2012).
- [63] K. Kasamatsu, M. Tsubota, and M. Ueda, Int. J. Mod. Phys. B **19**, 1835 (2005).
- [64] L. Cao, V. Bolsinger, S. I. Mistakidis, G. M. Koutentakis, S. Krönke, J. M. Schurer, and P. Schmelcher, J. Chem. Phys. **147**, 044106 (2017).
- [65] L. Cao, S. Krönke, O. Vendrell, and P. Schmelcher, J. Chem. Phys. **139**, 134103 (2013).
- [66] S. Krönke, L. Cao, O. Vendrell, and P. Schmelcher, New J. Phys. **15**, 063018 (2013).
- [67] See Supplemental Material at [URL].
- [68] M. O. Scully, and M. S. Zubairy, *Quantum optics*, cambridge university press. Cambridge, CB2 2RU, UK (1997).
- [69] S. I. Mistakidis, G. M. Koutentakis, G. C. Katsimiga, Th. Busch, and P. Schmelcher, arXiv: **1911.02011** (2019).
- [70] S. I. Mistakidis, A. G. Volosniev, and P. Schmelcher, arXiv: **1911.05353** (2019).
- [71] S. I. Mistakidis, G. C. Katsimiga, P. G. Kevrekidis, and P. Schmelcher, New J. Phys. **20**, 043052 (2018).
- [72] For typical axial confinement $\omega_x \approx 100\text{Hz}$, $100 < t_d < 300$ corresponds to $1 < t_d < 3$ s.
- [73] S. I. Mistakidis, L. Cao, and P. Schmelcher, J. Phys. B: At. Mol. and Opt. Phys. **47**, 225303 (2014).
- [74] V. Hakim, Phys. Rev. E **55**, 2835 (1997).
- [75] G. C. Katsimiga, S. I. Mistakidis, G. M. Koutentakis, P. G. Kevrekidis, and P. Schmelcher, Phys. Rev. A **98**, 013632 (2018).
- [76] P. Engels, and C. Atherton, Phys. Rev. Lett. **99**, 160405 (2007).
- [77] J. Levinsen, M. M. Parish, R. S. Christensen, J. J. Arlt, and G. M. Bruun, Phys. Rev. A **96**, 063622 (2017).
- [78] B. Field, J. Levinsen, and M. M. Parish, arXiv: **1910.02620** (2019).
- [79] P. E. Dolgirev, M. H. Michael, A. Zong, N. Gedik, and E. Demler, arXiv: **1910.02518** (2019).

Supplemental Material: Pump Probe Spectroscopy of Polarons and Evidence for Thermalization

DETAILS OF THE REVERSE RADIOFREQUENCY SPECTROSCOPY

Let us elaborate on the model that allows for the simulation of the MB dynamics under the influence of radiofrequency fields [S1, S2]. This model has been employed in the main text for the characterization of the coherence properties of polaronic quasiparticles in the context of pump-probe spectroscopy.

In our case few atomic impurities are immersed in a BEC environment close to an interspecies magnetic Feshbach resonance [S3]. The case of bosonic impurities possessing equal mass to the BEC atoms can be realized by employing different hyperfine states of a particular isotope e.g. ^{85}Rb or ^{87}Rb . For fermionic impurities the equal mass scenario occurs approximately e.g. for ^{173}Yb impurities immersed in a ^{174}Yb BEC with mass ratio of $m_B/m_I \approx 1.006$. Different masses for the impurities and the BEC atoms can be realized by invoking different atomic species, e.g. considering ^{87}Rb and ^{133}Cs [S4]. Typically, atoms close to a broad Feshbach resonance experience a sizeable quadratic Zeeman shift or are close to the Paschen-Back regime [S3]. For instance Feshbach resonances occur at magnetic fields of the order of 800 G for ^{85}Rb atoms where for comparison the Paschen-Back regime for the ground state $5^2S_{1/2}$ occurs for $B > 2000$ G [S5]. This sizeable Zeeman shift allows us to address selectively the distinct m_F transitions provided that the intensity of the radiofrequency pulse results in a Rabi frequency Ω_R much smaller than the Zeeman splitting of the involved hyperfine levels. The latter, is typically of the order of a few tenths of MHz. This large splitting of the different m_F levels implies that magnetic phenomena such as spin-exchange interactions can be safely neglected for these values of the magnetic field.

In this work we consider two hyperfine levels of the impurity atoms denoted as $|\uparrow\rangle$ and $|\downarrow\rangle$. These states can be identified and resonantly coupled for a frequency ν_0 , corresponding to the Zeeman splitting between the two levels, when a BEC environment is absent. Due to the harmonic confinement of the atoms each of the hyperfine levels is further divided into states of different atomic motion. The average spacing between these sublevels is of the order of the harmonic trap frequency, ω lying within the range of a few tenths of Hz to a few kHz in typical ultracold atom experiments [S6, S7]. In the vicinity of a Feshbach resonance the energy of these sublevels strongly depends on the interspecies interaction strength g_{BI} , between the impurity atoms in the resonantly-interacting hyperfine state, and their BEC environment. Accordingly the energy of each motional state shifts by $\Delta_+(g_{BI})$,

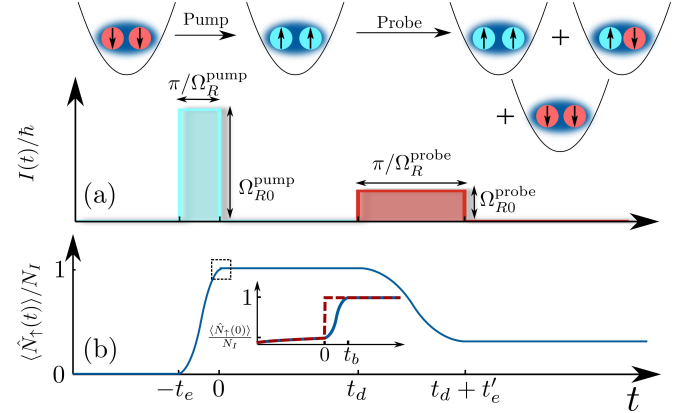


FIG. S1. (a) Schematic illustration of the employed PPS pulse sequences. The involved spin configuration at each state of the dynamics is also provided. (b) Expected time-evolution of the population of spin- \uparrow atoms during the PPS sequence. The inset depicts the evolution of $\langle \hat{N}_\uparrow(t) \rangle / N_I$ during the application of the optical burst pulse (blue line) and the approximation of employing the projection operator \hat{P} at $t = 0$ (dark red line).

from the corresponding non-interacting one. As it is also made obvious within the main text [see Fig. 1 (b)] this shift is of the order of $\sim \omega$ to $\sim 10\omega$. Therefore, due to the separation of the different involved energy scales it suffices to treat the impurities as two-level atoms. Furthermore, even for $\Omega_{R0} \gtrsim \Delta_+ \sim \text{kHz}$ where the regime of strong intense pulses is accessed, $\Omega_{R0} \ll \nu_0 \sim 10 \text{ MHz}$, allowing us to invoke the rotating wave approximation. Within this approximation and in the interaction picture of the $|\uparrow\rangle \leftrightarrow |\downarrow\rangle$ transition, the Hamiltonian for the internal state of the impurities reads $\hat{H}_S = -\frac{\hbar\Delta}{2}\hat{S}_z + \frac{\hbar\Omega_{R0}}{2}\hat{S}_x$, which is exactly the form employed in Eq. (1) of the main text. Ω_{R0} and $\Delta = \nu - \nu_0$ refer respectively to the (bare) Rabi frequency and the detuning with respect to the resonance of the $|\uparrow\rangle \leftrightarrow |\downarrow\rangle$ transition at $g_{BI} = 0$. We remark that the $|\uparrow\rangle$ and $|\downarrow\rangle$ states in the Schrödinger and interaction pictures are equivalent, so our conclusions are invariant under this frame transformation [S8].

To populate the polaronic states we employ the pump pulse of rectangular shape as depicted in Fig. S1 (a). The system is initialized in the non-interacting ground state where the impurity atoms are spin-polarized in their $|\downarrow\rangle$ state. The pump pulse is characterized by frequency ν^{pump} , and a detuning Δ^{pump} is employed. This pulse is further characterized by an exposure time t_e and a bare Rabi-frequency $\Omega_{R0}^{\text{pump}}$. Different realizations utilize different detunings Δ^{pump} and exposure times t_e but the same $\Omega_{R0}^{\text{pump}}$. In the duration of the pulse the sys-

tem undergoes Rabi-oscillations which for strong enough pulses $\Omega_{R0}^{\text{pump}} \gg \omega$ are well characterized by a Rabi-frequency $\Omega_R(\Delta^{\text{pump}}) = \sqrt{(\Omega_{R+}^{\text{pump}})^2 + (\Delta^{\text{pump}} - \Delta_+)^2}$, where $\Omega_{R+}^{\text{pump}}$ and Δ_+ are the corresponding resonance values. By fitting the spectroscopic signal, which is the fraction of atoms transferred to the $|\uparrow\rangle$ hyperfine state, to the theoretical lineshape for rectangular pulses reading

$$\frac{\langle \hat{N}_\uparrow(t) \rangle}{N_I} = \left[\frac{\Omega_{R+}^{\text{pump}}}{\Omega_R^{\text{pump}}(\Delta^{\text{pump}})} \right]^2 \sin^2 \left(\frac{\Omega_R^{\text{pump}}(\Delta^{\text{pump}})t_e}{2} \right), \quad (\text{S1})$$

these resonance values of $\Omega_{R+}^{\text{pump}}$ and Δ_+ can be obtained. Note here that the lineshape [Eq. (S1)] exhibits an infinite sequence of peaks at the locations, Δ_n^{pump} , $n = 0, \pm 1, \dots$, given by the solutions of

$$\frac{\Omega_R^{\text{pump}}(\Delta^{\text{pump}})t_e}{2} = \tan \left(\frac{\Omega_R^{\text{pump}}(\Delta^{\text{pump}})t_e}{2} \right) \quad (\text{S2})$$

for Δ^{pump} . Solving numerically Eq. (S2) we can identify the location of the three first peaks at positions $\Delta_0^{\text{pump}} = \Delta_+$ and $\Delta_{\pm 1}^{\text{pump}} \approx \Delta_+ \pm \Omega_{R+}^{\text{pump}} \sqrt{\left(\frac{8.9868}{\Omega_{R+}^{\text{pump}}t_e}\right)^2 - 1}$. Their corresponding amplitudes read $A_0 = \sin^2(\frac{1}{2}\Omega_{R+}^{\text{pump}}t_e)$ and $A_{\pm 1} \approx 0.01179(\Omega_{R+}^{\text{pump}}t_e)^2$. In order to achieve a high spectroscopic signal, $\langle \hat{N}_\uparrow(t_d) \rangle / N_I$, we set the exposure time to $t_e = \pi / \Omega_{R+}^{\text{pump}}$ (up to the obtained fitting accuracy) ensuring that $A_0 \approx 1$. This choice implies that the peaks at $\Delta_{\pm 1}^{\text{pump}}$ are clearly imprinted in the obtained spectrum possessing an amplitude $A_{\pm 1} \approx 0.116438$. Indeed, these side-peaks can be clearly identified in Fig. S1(b).

To infer the coherence properties of the polaronic states we employ pump-probe spectroscopy, see Fig. S1(b). Initially, we prepare the system in the same non-interacting ground state as in the previously examined protocol and apply a rectangular π -pulse, with $\Omega_{R0}^{\text{pump}} = 10$ and $t_e = \pi / \Omega_{R+}^{\text{pump}}$ on a polaronic resonance where we have identified the resonant $\Omega_{R+}^{\text{pump}}$ and Δ_+^{pump} as explained above. This sequence transfers the atoms from the ground state to the polaronic state in a very efficient manner. Then the impurity atoms are projected to the spin- \uparrow state by employing an optical burst transition on the lowest hyperfine state $|\downarrow\rangle$ to an available P electronic level at $t = 0$ which essentially ejects all the spin- \downarrow atoms from the trap. This procedure has been simulated by the application of the operator $\hat{H}_P = -i\Gamma \int dx \hat{\Psi}_\downarrow^\dagger(x) \hat{\Psi}_\downarrow(x)$ over a short time interval t_b . We can numerically verify that for large $\Gamma > 100$ and small $t_b \ll \omega^{-1}$ (corresponding to the experimentally relevant values) the action of \hat{H}_P to the state after the pump pulse is equivalent to the projection of the impurity to the spin- \uparrow configuration. For this reason and for computational simplicity we employ the state $|\Psi(t=0^+)\rangle = \frac{\hat{P}|\Psi(t=0^-)\rangle}{\|\hat{P}|\Psi(t=0^-)\rangle\|}$ as an initial state for the subsequent time-evolution $t > 0$. Note that this sequence for

$\Omega_R^{\text{pump}} \ll \omega$ is approximately equivalent to an interaction quench, as the pump-pulse has almost no spectral selectivity due to the pronounced power-broadening of the radiofrequency transition, as $\Omega_R^{\text{pump}} \sim \Delta_+^{\text{pump}}$ and the fact that the out-of-equilibrium dynamics is effectively frozen due to the small time-scale $t_e = \pi / \Omega_R^{\text{pump}} \ll \omega^{-1}$. Indeed, these properties of the pump-pulse have been verified numerically for the selected parameters $\Omega_{R0}^{\text{pump}}$ and Δ^{pump} as the MB state after this pulse is found to possess a fidelity in excess of 90% to the initial one.

After the pump sequence is completed we let the system evolve in the absence of radiofrequency fields, $\Omega_{R0}^{\text{dark}} = 0$, for a dark time, t_d . Finally, we apply a second probe π -pulse with a smaller $\Omega_{R0}^{\text{probe}} = 1$ to the first one and varying Δ_+^{probe} to transfer the atoms from the polaronic to the initial ground state. The employed spectroscopic signal is the fraction of atoms that have been deexcited by the probe pulse (recall that within our scheme all of the particles are at t_d in the spin- \uparrow state) divided by the total number of impurities, $\frac{\langle \hat{N}_\downarrow(t_d) \rangle}{N_I}$. Note that a smaller $\Omega_{R0}^{\text{probe}}$, when compared to $\Omega_{R0}^{\text{pump}}$, is employed in order to reduce the power-broadening during the probe sequence and subsequently increase the resolution in terms of detuning. However, this value cannot be arbitrarily lowered since for decreasing probe intensities the frequency-resolution is increased at the expense of lower temporal-resolution. For such low intensities the motional state of the spin- \uparrow impurities is significantly altered during the application of the probe pulse. As a heuristic argument the relation $\delta\nu\delta t \approx \hbar$ that connects the temporal (δt) and spectral ($\delta\nu$) resolution is commonly employed [S9]. The value of $\Omega_{R0}^{\text{probe}} = 1$ is selected within this work as it consists of an adequate tradeoff between the spectral and the temporal resolution. Finally, owing to the rectangular shape of the probe pulse the exhibited lineshape of $\frac{\langle \hat{N}_\downarrow(t_d) \rangle}{N_I}$ is given by Eq. (S1) as long as the impurity is coherent, i.e. $|g^{(1)}(x, x'; t_d)| \approx 1$. Accordingly, in our analysis we attribute all fringes appearing in the spectra to the lineshape of a single resonance if the ratio of the amplitude of two neighboring peaks satisfies $\frac{A_{n+1}}{A_n} < 0.12$.

CHARACTERIZATION OF THE RELAXATION DYNAMICS

We next explicate our method for characterizing the relaxation dynamics occurring in our setup during the hold time t_d . To achieve this we employ the Eigenstate Thermalization Hypothesis (ETH) [S10, S11]. Within this framework it is assumed that after a quench, the finite subsystems of a larger extended system relax to a steady state reminiscent of thermal equilibrium. Here by fitting the time-averaged one-body density of the impurities to a thermal equilibrium one, we show that this

thermalization process explains the relaxed state of the impurities emanating for long times after the orthogonal-ity catastrophe of the polarons.

The relaxation of an isolated (closed) system is understood in terms of the principle of local equivalence [S12]. Within this framework as the thermodynamical limit is approached, i.e. the system size tends to infinity, the reduced density matrices of the involved few-particle subsystems at long times can be calculated in terms of the density matrix of a (generalized) Gibbs ensemble at thermal equilibrium. Indeed, if the only conserved quantity of the Hamiltonian is the total energy then it can be shown that these reduced density matrices can be calculated in terms of the equilibrium density matrix within the Gibbs ensemble

$$\hat{\rho}_{\text{Gibbs}} = \frac{1}{Z} e^{-\frac{\hat{H}}{k_B T_{\text{eff}}}}. \quad (\text{S3})$$

In Eq. (S3) Z is the partition function stemming from the normalization of the density matrix, i.e. $\text{Tr}[\hat{\rho}_{\text{Gibbs}}] = 1$. \hat{H} refers to the MB Hamiltonian and T_{eff} , k_B correspond to the effective temperature and the Boltzmann constant respectively. Of course, our setup exhibits also other conserved quantities than the total energy. Below we resort to the approximation of no further symmetries as it is the only case that explicit results showing the relaxation dynamics of the system are available within ETH [S12]. As we shall show later on, the aforementioned choice leads to an excellent agreement between our numerical findings and the relevant estimates provided by applying Eq. (S3). Within this approximation the effective temperature, T_{eff} , is fixed by the conserved value of the energy per particle in the thermodynamic limit (TL)

$$\lim_{\text{BEC} \rightarrow \text{TL}} \frac{\text{Tr}[\Psi(0)\langle\Psi(0)|\hat{H}]}{N_B} = \lim_{\text{BEC} \rightarrow \text{TL}} \frac{\text{Tr}[\hat{\rho}_{\text{Gibbs}}\hat{H}]}{N_B}. \quad (\text{S4})$$

Here, $\text{BEC} \rightarrow \text{TL}$ is defined as the limit where $N_B \rightarrow \infty$, $g_{BB} \rightarrow 0$, $N_B g_{BB} = \text{constant}$ and $g_{BI}/g_{BB} = \text{constant}$. Notice, however, that Eq. (S3) and Eq. (S4), are impractical for calculations since the eigenvalues and eigenstates of the full interacting Hamiltonian, \hat{H} , are required for the evaluation of the Gibbs ensemble of the $(N_B + N_I)$ MB ensemble which are difficult if not impossible to obtain. For this reason, we simplify the above-mentioned set of equations so as to obtain explicit results which can be subsequently compared with those obtained by the time-evolution of the $(N_B + N_I)$ MB system within the ML-MCTDHX approach.

Since we intend to employ the thermodynamic limit where the MF Gross-Pitaevskii treatment of the BEC is exact in the weak interaction limit [S13], it is reasonable to assume that the corresponding density operator of the Gibbs ensemble acquires the product form $\hat{\rho}_{\text{Gibbs}} = \hat{\rho}_{B;\text{Gibbs}}^{(N_B)} \otimes \hat{\rho}_{I;\text{Gibbs}}^{(N_I)}$. Recall that during the dark time all of the impurities are in their spin- \uparrow state. In this

case, the form of $\hat{\rho}_{I;\text{Gibbs}}$ is similar to Eq. (S3), namely

$$\hat{\rho}_{I;\text{Gibbs}}^{(N_I)} = \frac{1}{Z_{\uparrow}} e^{-\frac{\hat{H}_{\uparrow}^{\text{eff}}}{k_B T_{\text{eff}}}}, \quad (\text{S5})$$

where H_I^{eff} is an effective Hamiltonian that acts only on the impurity. Equation (S5) greatly simplifies the description of our system, since the density matrix of the impurity depends only on the eigenvectors and eigenvalues of a N_I -body effective Hamiltonian. To proceed further we specify the form of $\hat{H}_{\uparrow}^{\text{eff}}$. Within a zeroth-order approximation we assume that the BEC acts solely as a potential barrier for the impurities and as consequence their effective Hamiltonian reads

$$\hat{H}_{\uparrow}^{\text{eff}}(t) = - \sum_{i=1}^{N_I} \frac{\hbar^2}{2m_I} \frac{d^2}{dx_i^2} + \frac{1}{2} m_I \omega^2 x_i^2 + g_{BI} \rho_B^{(1)}(x_i; t). \quad (\text{S6})$$

Notice that this approximation for the effective potential is a simplification of the impurity problem. First it neglects, among others, the renormalization of the impurity's mass, $m_I \rightarrow m_I^{\text{eff}}$, due to the presence of the BEC [S14]. Second, the presence of induced-interactions between the impurities cannot be captured [S15].

The time-dependence of the Hamiltonian of Eq. (S6) implies a non-stationary state for the impurities. However, it is well-known that following an interaction quench the density of the BEC is only slightly perturbed by the motion of the impurities [S14-S16]. The latter justifies the substitution of the effective Hamiltonian by its time-averaged value $\hat{H}_{\uparrow}^{\text{eff}} = \lim_{T \rightarrow \infty} \frac{1}{T} \int dt \hat{H}_{\uparrow}^{\text{eff}}(t)$, since $\rho_B^{(1)}(x_i; t) \approx \lim_{T \rightarrow \infty} \frac{1}{T} \int_0^T dt \rho_B^{(1)}(x_i; t)$ for the density of the bath. By incorporating the above-mentioned approximations we obtain explicit forms for the one-body density of the impurity within the Gibbs ensemble, namely

$$\rho_{I;\text{Gibbs}}^{(1)}(x, x'; T_{\text{eff}}) = \sum_{i=1}^{\infty} n_i(T_{\text{eff}}) \phi_i(x) \phi_i^*(x'). \quad (\text{S7})$$

Here, $n_i(T_{\text{eff}})$ is the distribution function of the N_I particles and ϕ_i refers to the eigenstates of $\hat{H}_{\uparrow}^{\text{eff}}$ respectively. Due to the small number of impurities considered herein ($N_I = 1, 2$) both the fermionic and the bosonic impurities do not follow the appropriate, for $N_I \rightarrow \infty$, Fermi-Dirac or Bose-Einstein distributions. Instead, it can be shown that the relevant distribution in the case of a single-particle or two bosons is the Boltzmann distribution

$$n_i(T_{\text{eff}}) = Z(1)^{-1} \exp\left(-\frac{\epsilon_i}{k_B T_{\text{eff}}}\right), \quad (\text{S8})$$

with ϵ_i being the eigenvalues of $\hat{H}_{\uparrow}^{\text{eff}}$ and $Z(1) = \sum_{i=1}^{\infty} \exp\left(-\frac{\epsilon_i}{k_B T_{\text{eff}}}\right)$. For two-fermions the corresponding distribution reads

$$n_i(T_{\text{eff}}) = \left[\frac{Z(2) - e^{-\frac{\epsilon_i}{k_B T_{\text{eff}}}} (Z(1) - e^{-\frac{\epsilon_i}{k_B T_{\text{eff}}}}) e^{\frac{\epsilon_i}{k_B T_{\text{eff}}}}}{Z(1) - e^{-\frac{\epsilon_i}{k_B T_{\text{eff}}}}} + 1 \right]^{-1}, \quad (\text{S9})$$

where $Z(2) = \sum_{i=1}^{\infty} e^{-\frac{\epsilon_i}{k_B T_{\text{eff}}}} (Z(1) - e^{-\frac{\epsilon_i}{k_B T_{\text{eff}}}})$. Note also that the one-body density of the impurity, Eq. (S7), depends only on a single parameter namely the effective temperature, T_{eff} .

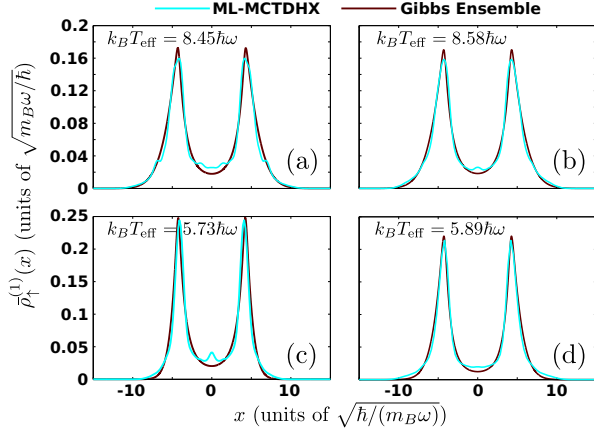


FIG. S2. The time-averaged one-body density, $\bar{\rho}_{\uparrow}^{(1)}(x)$ within the MB approach (light blue lines) compared to the best fit of the ETH model, $\rho_{\uparrow; \text{Gibbs}}^{(1)}(x; t_{\text{eff}})$ (dark red lines). Our results refer to (a) $N_I = 1$, (b) $N_I = 2$ bosonic and (c) $N_I = 2$ fermionic mass-balanced, $m_I = m_B$ impurities. (d) Corresponds to the case of $N_I = 2$ heavy, $m_I = 133/78 m_B$, bosonic impurities.

In the main text we have shown that the one-body density matrix of the impurities, $\rho_{\uparrow}^{(1)}(x, x'; t)$, saturates to its time-averaged value, i.e. $\rho_{\uparrow}^{(1)}(x, x'; t \rightarrow \infty) \approx \bar{\rho}_I^{(1)}(x, x') = \lim_{T \rightarrow \infty} \frac{1}{T} \int_0^T dt \rho_{\uparrow}^{(1)}(x, x'; t)$, for long hold times, as it is evident in the relaxation dynamics of $\Delta \bar{g}^{(1)}$ [see Fig. 2(e) in the main text]. In order to facilitate the comparison of our results to the ETH prediction [Eq. (S7)] we fit the averaged one-body density matrix, $\bar{\rho}_{\uparrow}^{(1)}(x, x')$, obtained within ML-MCTDHX to the corresponding Gibbs ensemble, $\rho_{\uparrow; \text{Gibbs}}^{(1)}(x, x'; T_{\text{eff}})$, and extract the value of T_{eff} . Our results for the best fitted parameters are shown in Fig. S2. We remark that the fitting is performed on the level of $\bar{\rho}_{\uparrow}^{(1)}(x, x')$, while only the diagonal $\bar{\rho}_{\uparrow}^{(1)}(x) \equiv \bar{\rho}_{\uparrow}^{(1)}(x, x)$ is presented in Fig. S2 in order to enhance the visibility of the obtained results. By comparing the time averaged one-body density and the fitted Gibbs ensemble prediction a very good agreement is observed, for both one [Fig. S2(a)] and two impurities of either bosonic [Fig. S2(b)] or fermionic [Fig. S2(c)] nature. This result holds equally also in the case of mass-imbalanced mixtures composed for instance of heavy bosonic impurities, $m_I = 133/78 m_B$ [see e.g. Fig. S2(d)]. The above findings indicate that despite the employed approximations the ETH scheme is able to capture the main features exhibited by the relaxed state of the impurities within our correlated MB system.

Regarding the effective temperature we find rather

large values of T_{eff} for one and two bosonic impurities that is of the order of $T_{\text{eff}} \approx 8/k_B$ harmonic units. Whilst for two fermions and two heavier bosonic impurities the temperature is slightly smaller possessing values of the order of $T_{\text{eff}} \approx 6/k_B$. These large values of the effective temperature are indicative of the incoherent character of the impurities after the probe pulse [see also Fig. 3(d) in the main text]. To advance further the correspondence between the ETH model and the correlated MB results we estimate the effective temperature of the relaxed state by expressing Eq. (S4) only in terms of the impurity's degrees of freedom. Notice that the energy of the impurity is not conserved during the MB evolution of our system due to the presence of energy exchange processes between the impurity and the bath. However, as evidenced in Fig. S3 below, the energy of the impurities saturates for large times (see also Section). Indeed, by taking advantage of this observation we can cast Eq. (S4) in the form

$$\bar{E}_{\uparrow} = \lim_{T \rightarrow \infty} \frac{1}{T} \int_0^T dt \langle \Psi(t) | \hat{H} - \hat{H}_B^0 - \hat{H}_{BB} | \Psi(t) \rangle \quad (\text{S10})$$

$$= \text{Tr} \left[\hat{\rho}_{\uparrow; \text{Gibbs}}^{(N_I)} \hat{H}_{\uparrow}^{\text{eff}} \right],$$

where \bar{E}_{\uparrow} is the time-averaged impurity energy. In the case of a single impurity, Eq. (S10) gives an estimation for the effective temperature of $T_{\text{eff}} = 8.56/k_B$ which is in good agreement with the effective temperature obtained by fitting $T_{\text{eff}} = 8.45/k_B$. Note also here that the effective Hamiltonian of Eq. (S6) is known to overestimate the zero-point energy of the impurity since it neglects its dressing by the excitations of the BEC [S14]. This in turn explains the higher T_{eff} obtained via Eq. (S10). In contrast, in the case of two impurities the related estimates for T_{eff} are much higher than the ones obtained by the fitting of $\bar{\rho}_{\uparrow}^{(1)}(x, x')$. Specifically, Eq. (S10) yields $T_{\text{eff}} = 10.28/k_B$ and $T_{\text{eff}} = 6.89/k_B$ for the two bosonic and the two fermionic impurities respectively. The observed discrepancy is attributed to the presence of induced interactions between the impurities that are more prevalent in the case of bosonic impurities than fermionic ones [S15]. However, their effect is neglected within the effective Hamiltonian of Eq. (S6).

INTERSPECIES INTERACTION ENERGY

To further support the thermalization tendency of the multicomponent system for strong impurity-BEC interactions at long times of the nonequilibrium dynamics we next inspect the behavior of the interspecies interaction energy. The latter quantity is defined as $\langle \hat{H}_{BI}(t) \rangle \equiv \langle \Psi(t) | \hat{H}_{BI} | \Psi(t) \rangle$, where the operator of the interspecies interactions is $\hat{H}_{BI} = g_{BI} \int dx \hat{\Psi}_B^{\dagger}(x) \hat{\Psi}_{\uparrow}^{\dagger}(x) \hat{\Psi}_{\uparrow}(x) \hat{\Psi}_B(x)$. Also, $\hat{\Psi}_{\sigma}(x)$ and $\hat{\Psi}_{\sigma}^{\dagger}(x)$ denote the σ -species field opera-

tor that annihilates and creates respectively a σ -species particle at position x .

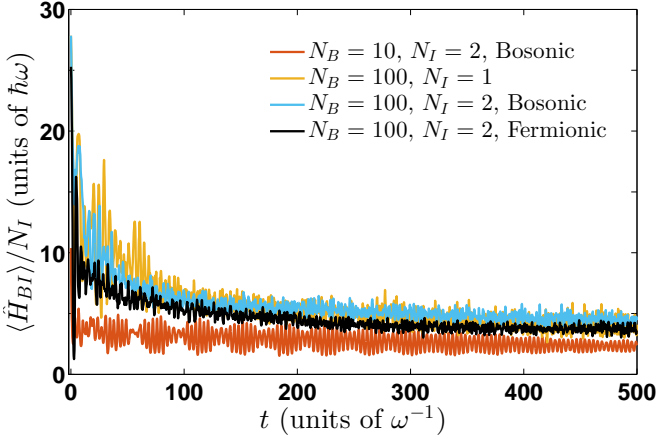


FIG. S3. Evolution of the impurity-BEC interaction energy per impurity particle applying a pump pulse to drive the impurities to the spin- \uparrow state with $g_{BI} = 1.5$ for a single ($N_I = 1$) and two ($N_I = 2$) bosonic or fermionic impurities and also for a few-body bath consisting of $N_B = 10$ particles (see legend). In all cases $g_{BB} = 0.5$ and $g_{II} = 0$.

The time-evolution of $\langle \hat{H}_{BI}(t) \rangle / N_I$ is illustrated in Fig. S3 upon considering a pumping that drives the atoms to the spin- \uparrow state with $g_{BI} = 1.5$. Specifically, we consider different settings consisting of $N_I = 1$, $N_I = 2$ spin-polarized bosons or fermions as well as a few-body system containing $N_B = 10$ bosons and $N_I = 2$ non-interacting impurities. In all cases we observe that $\langle \hat{H}_{BI}(t) \rangle / N_I$ decreases up to $t = 100$ while for later times, and in particular for $t > 200$, it shows a saturation trend to a certain value depending on both N_I and N_B . Recall that this saturation effect allowed for the derivation of Eq. (S9) within the ETH scheme. Notice also that the saturation value of $\langle \hat{H}_{BI}(t) \rangle / N_I$ is smaller for the few-body system ($N_B = 10$, $N_I = 2$) while for the $N_B = 100$ setups $\langle \hat{H}_{BI}(t) \rangle / N_I$ acquires its smaller value for two fermionic impurities and takes almost the same value for $N_I = 1$ and $N_I = 2$ non-interacting bosonic impurities. Finally, let us note that the overall decreasing behavior of $\langle \hat{H}_{BI}(t) \rangle / N_I$ suggests a transfer of energy from the impurities to the bosonic gas as it has been also demonstrated in Refs. [S14, S16]. This energy transfer process, identified by the decreasing rate of $\langle \hat{H}_{BI}(t) \rangle / N_I$, seems to be enhanced for $N_B = 10$ whilst for the $N_B = 100$ setups it is more pronounced for the fermionic impurities. We remark that a saturation trend at long time-scales being in turn suggestive of the thermalization tendency of the system occurs also for other observables. These include, for instance, the von-Neumann entropy [S16–S18] that quantifies the degree of entanglement or other entropic measures for the intraspecies correlations [S19, S20] (results not shown for brevity).

THE MANY-BODY VARIATIONAL METHODOLOGY: ML-MCTDHX

To track the stationary properties and most importantly the MB quantum dynamics of the multicomponent system addressed in the main text we resort to the Multi-Layer Multi-Configuration Time-Dependent Hartree method for atomic mixtures (ML-MCTDHX) [S21–S23]. It constitutes an ab-initio variational method for solving the time-dependent MB Schrödinger equation of atomic mixtures possessing either bosonic [S17, S24, S25] or fermionic [S8, S18, S26, S27] spinor components. A major advantage of this approach is the expansion of the total MB wavefunction with respect to a time-dependent and variationally optimized basis (see below). This allows us to capture all the relevant inter- and intraspecies correlations of a multicomponent system in an efficient manner at each time instant by utilizing a reduced number of basis states when compared to expansions relying on a time-independent basis.

The system considered in the main text consists of a bosonic bath (B) with $N_B = 100$ atoms and either one ($N_I = 1$) or two ($N_I = 2$) impurity (I) atoms. Most importantly, the impurities being either bosons or fermions possess an internal pseudospin-1/2 degree of freedom [S14, S28]. To account for interspecies correlations, the MB wavefunction $|\Psi(t)\rangle$ is expressed according to a truncated Schmidt decomposition [S17, S24, S29] in terms of D different species functions, i.e. $|\Psi_k^\sigma(t)\rangle$, for each component $\sigma = B, I$. We remark that the time-dependent species functions $|\Psi_k^\sigma(t)\rangle$ form an orthonormal N_σ -body wavefunction set within a subspace of the σ -species Hilbert space \mathcal{H}^σ [S21]. Then, the MB wavefunction $|\Psi(t)\rangle$ ansatz reads

$$|\Psi(t)\rangle = \sum_{k=1}^D \sqrt{\lambda_k(t)} |\Psi_k^B(t)\rangle |\Psi_k^I(t)\rangle, \quad (\text{S11})$$

where the time-dependent Schmidt weights $\lambda_k(t)$ are also known as the natural species populations of the k -th species function and provide information about the degree of entanglement between the individual subsystems. For instance, if two different $\lambda_k(t)$ are nonzero then $|\Psi(t)\rangle$ is a linear superposition of two states and therefore the system is entangled [S29, S30] or interspecies correlated. On the other hand, in the case of $\lambda_1(t) = 1$, $\lambda_{k>1}(t) = 0$, the wavefunction is a direct product of two states and the system is non-entangled.

Next, in order to include intraspecies correlations into our MB wavefunction ansatz each species function $|\Psi_k^\sigma(t)\rangle$ is further expanded on a time-dependent number-state basis set $|\vec{n}(t)\rangle^\sigma$. Namely

$$|\Psi_k^\sigma(t)\rangle = \sum_{\vec{n}} A_{k;\vec{n}}^\sigma(t) |\vec{n}(t)\rangle^\sigma, \quad (\text{S12})$$

where $A_{k;\vec{n}}^\sigma(t)$ denote the underlying time-dependent ex-

pansion coefficients. Moreover, each number state $|\vec{n}(t)\rangle^\sigma$ corresponds to a permanent for bosons or a determinant for fermions building upon d^σ time-dependent variationally optimized single-particle functions (SPFs) i.e. $|\phi_l^\sigma(t)\rangle$, $l = 1, 2, \dots, d^\sigma$ being characterized by occupation numbers $\vec{n} = (n_1, \dots, n_{d^\sigma})$. Additionally, the SPFs are expanded with respect to a time-independent primitive basis. For the majority species, this primitive basis corresponds to an \mathcal{M} dimensional discrete variable representation denoted in the following by $\{|q\rangle\}$. However, for the impurities the primitive basis refers to the tensor product $\{|q, s\rangle\}$ of the discrete variable representation basis regarding the spatial degrees of freedom and the two-dimensional pseudospin-1/2 basis $\{|\uparrow\rangle, |\downarrow\rangle\}$. Consequently, each SPF of the impurities acquires the following spinor wavefunction form

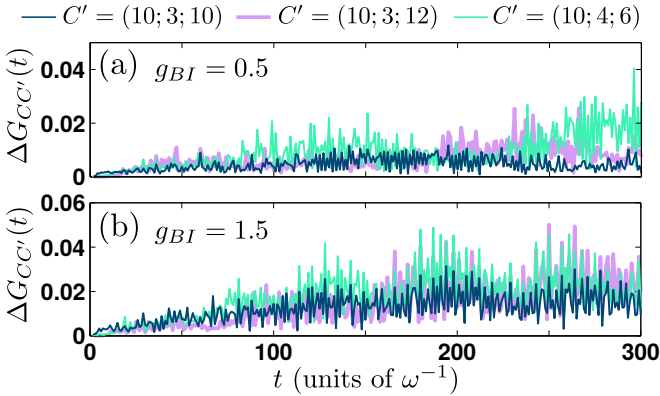


FIG. S4. Evolution of the one-body coherence absolute deviation $\Delta G_{C,C'}(t)$ between the $C = (10; 3; 8)$ and other orbital configurations $C' = (D; d^B; d^I)$ (see legend) for (a) $g_{BI} = 0.5$ and (b) $g_{BI} = 1.5$. In all cases $N_B = 100$, $N_I = 2$ with $g_{BB} = 0.5$ and $g_{II} = 0$ while initially $g_{BI} = 0$.

$$|\phi_j^I(t)\rangle = \sum_{q=1}^{\mathcal{M}} (B_{jq\uparrow}^I(t) |q\rangle |\uparrow\rangle + B_{jq\downarrow}^I(t) |q\rangle |\downarrow\rangle). \quad (\text{S13})$$

Here, $B_{jq\uparrow}^I(t)$ [$B_{jq\downarrow}^I(t)$] are the time-dependent expansion coefficients of the pseudospin- \uparrow and \downarrow respectively, see also Refs. [S8, S14].

Having exemplified the MB wavefunction ansatz and in order to address the time-evolution of the $(N_B + N_I)$ -body wavefunction $|\Psi(t)\rangle$ obeying the Hamiltonian of Eq. (1) of the main text we then numerically solve the so-called ML-MCTDHX equations of motion [S21]. These equations are determined by following the Dirac-Frenkel [S31, S32] variational principle for the generalized ansatz of Eqs. (S11), (S12) and (S13). In this way, we obtain a set of D^2 linear differential equations of motion for the $\lambda_k(t)$ coefficients coupled to $D(\frac{(N_B+d^B-1)!}{N_B!(d^B-1)!} + \frac{(N_I+d^I-1)!}{N_I!(d^I-1)!})$ nonlinear integrodifferential equations for the species functions and $d^B + d^I$ nonlinear integrodifferential equations for the SPFs.

CONVERGENCE OF THE MANY-BODY SIMULATIONS

The Hilbert space truncation within the ML-MCTDHX method is determined by the considered orbital configuration space i.e. $C = (D; d^B; d^I)$. In this notation, $D = D^B = D^I$ and d^B , d^I denote the number of species functions and SPFs respectively of each species [Eqs. (S11) and (S12)]. Moreover, within our numerical calculations we employ a primitive basis based on a sine discrete variable representation for the spatial part of the SPFs with $\mathcal{M} = 600$ grid points. This sine discrete variable representation intrinsically introduces hard-wall boundary conditions at both edges of the numerical grid which in our case are located at $x_{\pm} = \pm 50$. We assured that the location of the hard-wall boundaries does not impact our findings since no significant density portion occurs beyond $x_{\pm} = \pm 20$. The eigenstates of the multicomponent system are obtained by utilizing the so-called improved relaxation method [S21–S23] within ML-MCTDHX. To address the corresponding nonequilibrium dynamics, we numerically solve the ML-MCTDHX equations of motion using the MB wavefunction [Eq. (S11)] under the influence of the Hamiltonian (1) of the main text.

To testify the convergence of the MB results we ensured that all observables of interest are to a certain level of accuracy insensitive for a varying orbital configuration space, $C = (D; d^B; d^I)$. Note that for the MB simulations discussed in the main text we relied on the orbital configuration $C = (10; 3; 8)$. To infer the convergence of our results we exemplarily showcase below the behavior of the spatially integrated one-body coherence function $g^{(1)}(x, x'; t)$ for different number of species and single-particle functions in the course of time. In particular we calculate its normalized absolute deviation between the $C = (10; 3; 8)$ and other orbital configurations $C' = (D; d^B; d^I)$, namely

$$\Delta G_{C,C'}(t) = \frac{\int dx dx' |g_C^{(1)}(x, x'; t) - g_{C'}^{(1)}(x, x'; t)|}{\int dx dx' g_C^{(1)}(x, x'; t)}. \quad (\text{S14})$$

The dynamics of $\Delta G_{C,C'}(t)$ is illustrated in Fig. S4 for the multicomponent bosonic system consisting of $N_B = 100$ atoms and $N_I = 2$ non-interacting impurities upon considering the pump spectroscopic sequence introduced in Section from $g_{BI} = 0$ either to $g_{BI} = 0.5$ [Fig. S4(a)] or towards $g_{BI} = 1.5$ [Fig. S4(b)]. Evidently, a systematic convergence of $\Delta G_{C,C'}(t)$ is achieved in both cases. Indeed, closely inspecting $\Delta G_{C,C'}(t)$ for $g_{BI} = 0.5$ we observe that the deviation between the $C = (10; 3; 8)$ and $C' = (10; 4; 6)$ [$C' = (10; 3; 10)$] orbital configurations remains below 3.8% [1.2%] in the entire time-evolution [Fig. S4(a)]. On the other hand, for increasing g_{BI} $\Delta G_{C,C'}(t)$ takes larger values, as shown in Fig. S4(b).

For instance, at $g_{BI} = 1.5$ the relative error $\Delta G_{C,C'}(t)$ with $C = (10; 3; 8)$ and $C' = (10; 4; 6)$ [$C' = (10; 3; 10)$] becomes at most of the order of 5.2% [3%] at long evolution times $t > 150$. It is also worth mentioning at this point that for all other observables and interspecies interaction strengths discussed in the main text a similar degree of convergence takes place (results not shown here for brevity).

-
- [S1] C. Kohstall, M. Zaccanti, M. Jag, A. Trenkwalder, P. Massignan, G. M. Bruun, F. Schreck, and R. Grimm, *Nature* **485**, 615 (2012).
- [S2] F. Scazza, G. Valtolina, P. Massignan, A. Recati, A. Amico, A. Burchianti, C. Fort, M. Inguscio, M. Zaccanti, and G. Roati, *Phys. Rev. Lett.* **118**, 083602 (2017).
- [S3] C. Chin, R. Grimm, P. Julienne, and E. Tiesinga, *Rev. Mod. Phys.* **82**, 1225 (2010).
- [S4] M. Hohmann, F. Kindermann, B. Gnger, T. Lausch, D. Mayer, F. Schmidt, and A. Widera, *EPJ Quantum Technology* **2**, 23 (2015).
- [S5] D. A. Steck, Rubidium 85 D Line Data, <http://steck.us/alkalidata> (2013).
- [S6] A. Amico, F. Scazza, G. Valtolina, P. E. S. Tavares, W. Ketterle, M. Inguscio, G. Roati, and M. Zaccanti, *Phys. Rev. Lett.* **121**, 253602 (2018).
- [S7] M. A. Hoefer, J. J. Chang, C. Hamner, and P. Engels, *Phys. Rev. A* **84**, 041605(R) (2011).
- [S8] G. M. Koutentakis, S. I. Mistakidis, and P. Schmelcher, *New J. Phys.* **21**, 053005 (2019).
- [S9] J. J. Sakurai, *Advanced Quantum Mechanics*, Pearson (1967).
- [S10] M. Rigol and M. Srednicki, *Phys. Rev. Lett.* **108**, 110601 (2012).
- [S11] M. Rigol, V. Dunjko, and M. Olshanii, *Nat.* **452**, 854 (2008).
- [S12] F. H. L. Essler and M. Fagotti, *J. Stat. Mech.* **6** 064002 (2016).
- [S13] C. J. Pethick, and H. Smith, *Bose-Einstein condensation in dilute gases*, Cambridge University press (Cambridge 2002).
- [S14] S. I. Mistakidis, G. C. Katsimiga, G. M. Koutentakis, Th. Busch, and P. Schmelcher, *Phys. Rev. Lett.* **122**, 183001 (2019).
- [S15] S. I. Mistakidis, G. M. Koutentakis, G. C. Katsimiga, Th. Busch, and P. Schmelcher, *arXiv: 1911.02011* (2019).
- [S16] S. I. Mistakidis, F. Grusdt, G. M. Koutentakis, and P. Schmelcher, *New J. Phys.* **21**, 103026 (2019).
- [S17] S. I. Mistakidis, G. C. Katsimiga, P. G. Kevrekidis, and P. Schmelcher, *New J. Phys.* **20**, 043052 (2018).
- [S18] J. Erdmann, S. I. Mistakidis, and P. Schmelcher, *Phys. Rev. A* **99**, 013605 (2019).
- [S19] S. Bera, B. Chakrabarti, A. Gammal, M. C. Tsatsos, M. L. Lekala, B. Chatterjee, C. L  v  que and A. U. J. Lode, *arXiv:1806.02539* (2018).
- [S20] R. Roy, A. Gammal, M. C. Tsatsos, B. Chatterjee, B. Chakrabarti, and A. U. Lode, *Phys. Rev. A* **97**, 043625 (2018).
- [S21] L. Cao, V. Bolsinger, S. I. Mistakidis, G. M. Koutentakis, S. Kr  nke, J. M. Schurer, and P. Schmelcher, *J. Chem. Phys.* **147**, 044106 (2017).
- [S22] L. Cao, S. Kr  nke, O. Vendrell, and P. Schmelcher, *J. Chem. Phys.* **139**, 134103 (2013).
- [S23] S. Kr  nke, L. Cao, O. Vendrell, and P. Schmelcher, *New J. Phys.* **15**, 063018 (2013).
- [S24] G. C. Katsimiga, G. M. Koutentakis, S. I. Mistakidis, P. G. Kevrekidis, and P. Schmelcher, *New J. Phys.* **19**, 073004 (2017).
- [S25] S. I. Mistakidis, A. G. Volosniev, N. T. Zinner, and P. Schmelcher, *Phys. Rev. A* **100**, 013619 (2019).
- [S26] P. Siegl, S. I. Mistakidis, and P. Schmelcher, *Phys. Rev. A* **97**, 053626 (2018).
- [S27] S. I. Mistakidis, G. C. Katsimiga, G. M. Koutentakis, and P. Schmelcher, *New J. Phys.* **21**, 043032 (2019).
- [S28] K. Kasamatsu, M. Tsubota, and M. Ueda, *Int. J. Mod. Phys. B* **19**, 1835 (2005).
- [S29] R. Horodecki, P. Horodecki, M. Horodecki, and K. Horodecki, *Rev. Mod. Phys.* **81**, 865 (2009).
- [S30] M. Roncaglia, A. Montorsi, and M. Genovese, *Phys. Rev. A* **90**, 062303 (2014).
- [S31] J. Frenkel, in *Wave Mechanics* 1st ed. (Clarendon Press, Oxford, 1934), pp. 423-428.
- [S32] P. A. Dirac, *Proc. Camb. Phil. Soc.*, **26**, 376, Cambridge University Press (1930).